Chinese Chemical Letters 33 (2022) 957–962

Contents lists available at ScienceDirect

Chinese Chemical Letters

journal homepage: www.elsevier.com/locate/cclet

Tuning the shell thickness of core-shell α-Fe_2O_3@SiO_2 nanoparticles to promote microwave absorption

Honghong Fu[a,1], Yue Guo[c,1], Jian Yu[d,1], Zhen Shen[c], Jie Zhao[a,c,*], Yu Xie[a], Yun Ling[a], Sheng Ouyang[b], Shiqi Li[a], Wei Zhang[e,*]

[a] Department of Materials Chemistry, School of Environment and Chemical Engineering, Nanchang Hangkong University, Nanchang 330063, China
[b] Instrumental Analysis Center of Nanchang Hangkong University, Nanchang 330063, China
[c] School of Chemistry and Chemical Engineering, Nanjing University, Nanjing 210023, China
[d] Research Institute of Aero-Engine, Beihang University, Beijing 100191, China
[e] School of Ecology and Environment, Zhengzhou University, Zhengzhou 450001, China

ARTICLE INFO

Article history:
Received 9 April 2021
Revised 6 June 2021
Accepted 8 July 2021
Available online 15 July 2021

Keywords:
α-Fe_2O_3@SiO_2
Core-shell structure
Microwave absorption
Dielectric loss
Interfacial polarization
Conductivity loss

ABSTRACT

Various advanced microwave absorbing materials have been developed for reducing/avoiding the harm of microwave radiation. Among them, core-shell structural nanomaterials have been widely fabricated for microwave absorption. However, the "structure-performance" relationship between shell thickness and microwave absorption performance is rarely reported. In this paper, we first explored the "structure-performance" relationship between shell thickness and microwave absorption performance, based on the core-shell α-Fe_2O_3@SiO_2 nanoparticles with a constant α-Fe_2O_3-core size and changeable SiO_2-shell thickness. With increasing the SiO_2-shell thickness, the microwave absorption ability first increased, then decreased. Under a proper SiO_2-shell thickness of 35 nm, α-Fe_2O_3@SiO_2 sample achieved the strongest microwave absorbing ability with a reflection loss minimum value of –4.3 dB, better than that of pure α-Fe_2O_3 (–3.8 dB). This enhanced microwave absorption performance was mainly derived from the dielectric loss. Although the absolute value of the reflection loss was relatively low (–4.3 dB), this study shed an important reference on designing next-generation advanced iron oxide-based materials for microwave absorption.

With more and more electronic products into life, the microwave radiation generated by electronic devices has caused harm to human health and the environment. In order to reduce/avoid the harm of microwave radiation, intensive efforts have been made to develop advanced microwave absorbing materials [1-5]. At present, the widely used microwave absorbing materials are mainly divided into ferrites (Fe_3O_4, α-Fe_2O_3 and $BaFe_{12}O_{19}$, *etc.*) [6-8], magnetic metals (Ni, Co, α-Fe) [9-11], non-iron-based metal oxides (TiO_2, NiO, $CaBiNb_2O_4$, ZnO and MoS_2, *etc.*) [12-16], carbon-based materials (graphene, carbon nanotube and porous carbon, *etc.*) [17-20], polymers (polyaniline, polypyrrole, and polythiophene, *etc.*) [21-23], and other composites [24-31]. Among them, ferrites have attracted extensive interest owing to their abundant resources, low cost, and good absorption performance [32,33].

Usually, ferrites have three structures, *i.e.*, Fe_3O_4, γ-Fe_2O_3 and α-Fe_2O_3. Among them, Fe_3O_4 and γ-Fe_2O_3 belong to ferromagnetic materials, which have large saturation magnetization and high relative complex permeability suiting for microwave absorption. However, these two ferrites are easy to oxidization and agglomerate, leading to poor microwave absorption performance [2,34]. By contrast, α-Fe_2O_3 provides more options for the microwave absorber design due to its stable chemical properties, environment-friendly feature, and controllable morphology.

Various morphologies of α-Fe_2O_3 have been widely reported, such as microspheres, microcubes, nanoparticles, and nanorods [35-42]. Coating an insulating layer on α-Fe_2O_3 particle surface is an effective strategy to adjust the particle-particle distance, enhance the anti-oxidation capability, reduce the density of particles, and improve the impedance matching between particles and free space. As a surface modification material, SiO_2 is an ideal candidate due to its excellent chemical stability, nontoxicity, and easy conjugation with various functional groups. Various structures with α-Fe_2O_3 as the core and SiO_2 as the shell have been fabricated for microwave absorption, such as core-shell structure, and yolk-

* Corresponding authors.
E-mail addresses: zhaojienju@163.com (J. Zhao), xieyu_121@163.com (Y. Xie), lqfoys@163.com (S. Ouyang), zhangwei88@zzu.edu.cn (W. Zhang).
[1] These authors contributed equally to this work and should be considered as co-first authors.

https://doi.org/10.1016/j.cclet.2021.07.027
1001-8417/

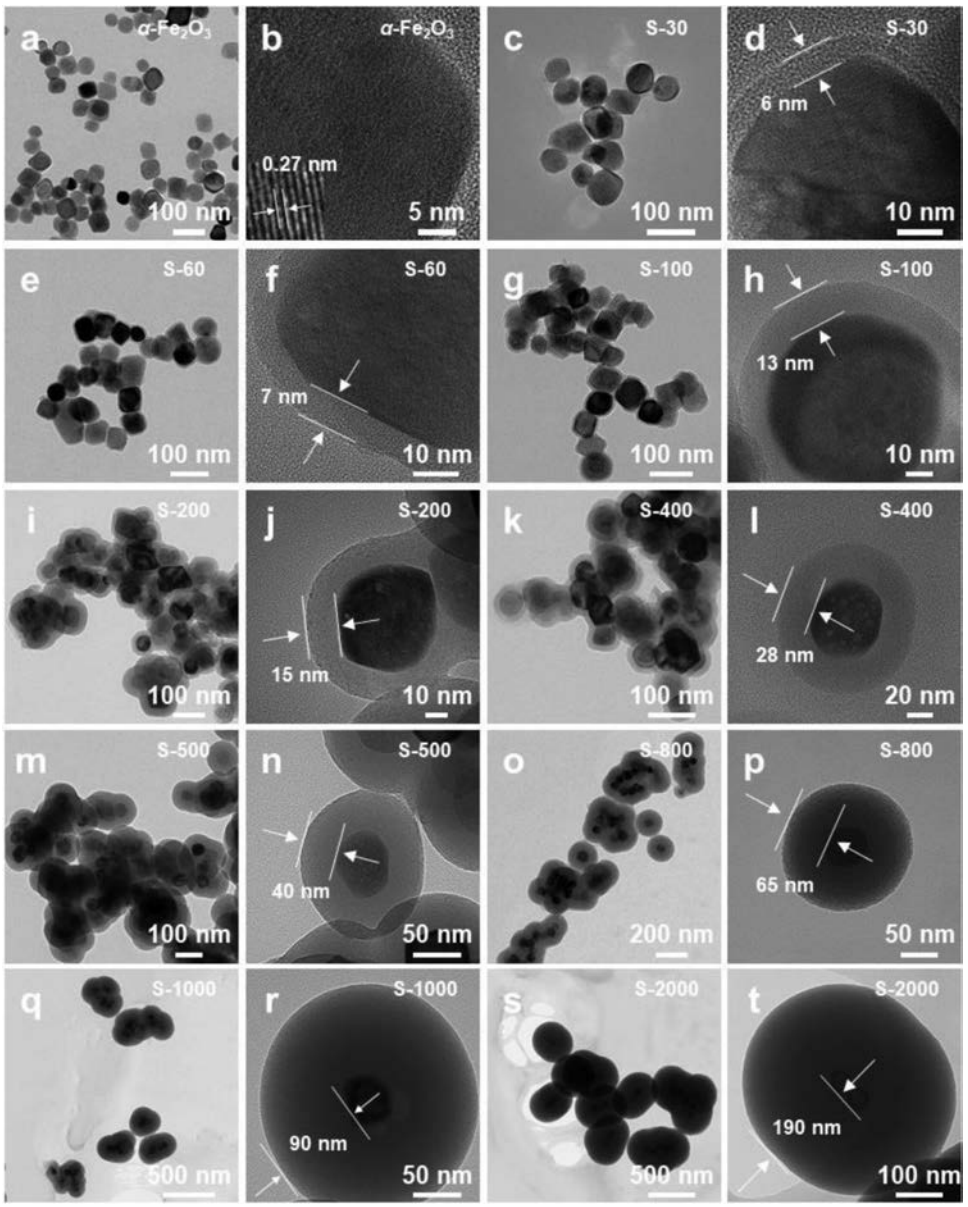

Fig. 1. Regulation of shell-thickness in core-shell structural α-Fe_2O_3@SiO_2 nanoparticles: (a, b) α-Fe_2O_3, (c, d) S-30, (e, f) S-60, (g, h) S-100, (i, j) S-200, (k, l) S-400, (m, n) S-500, (o, p) S-800, (q, r) S-1000, (s, t) S-2000.

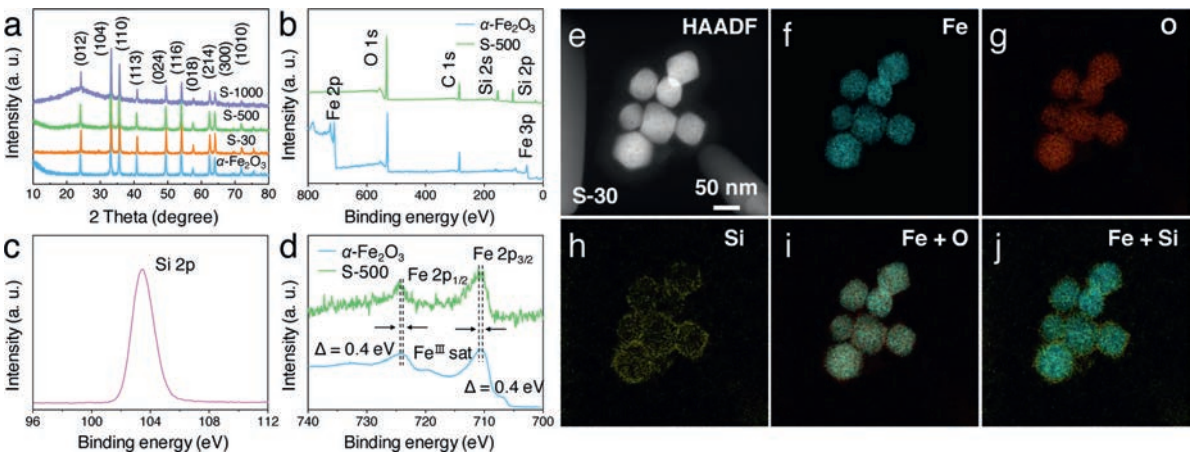

Fig. 2. Structure and components characterization. (a) XRD patterns. (b) XPS full spectra. (c,d) XPS fine spectra of Si 2p and Fe 2p. (e) High-angle annular dark-field (HAADF) image. (f-j) Elemental mappings of Fe, O, Si, Fe + O, and Fe + Si.

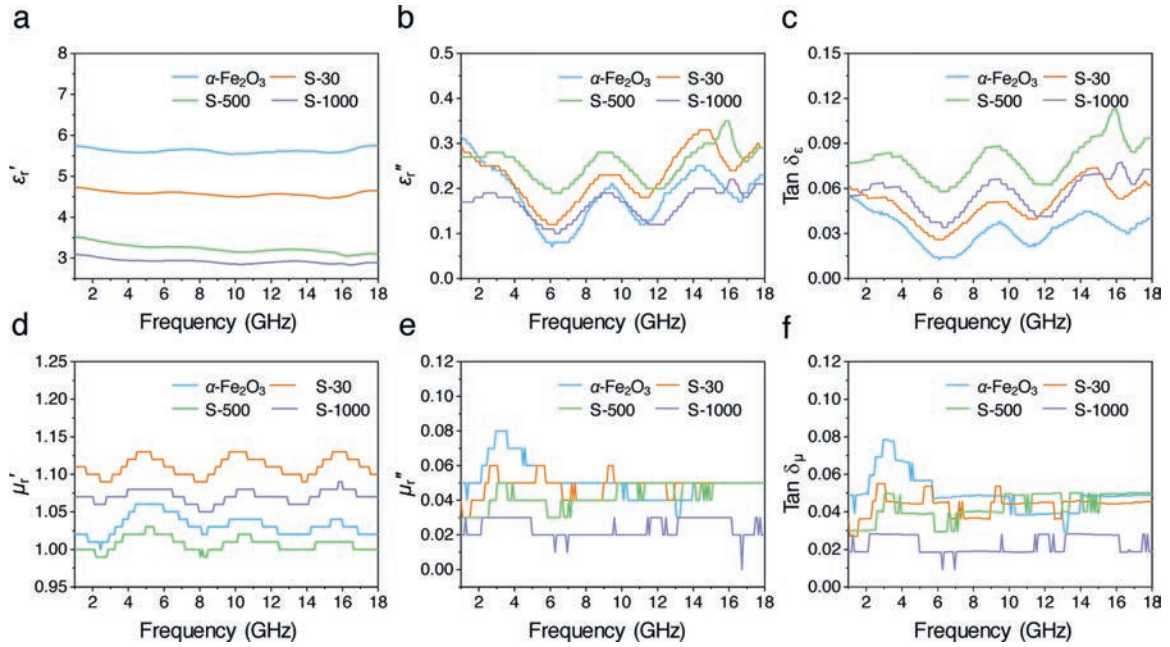

Fig. 3. Electromagnetic parameters: (a) ε_r', (b) ε_r'', (c) tan ε_ε, (d) ε_r', (e) μ_r'', (f) tan δ_μ.

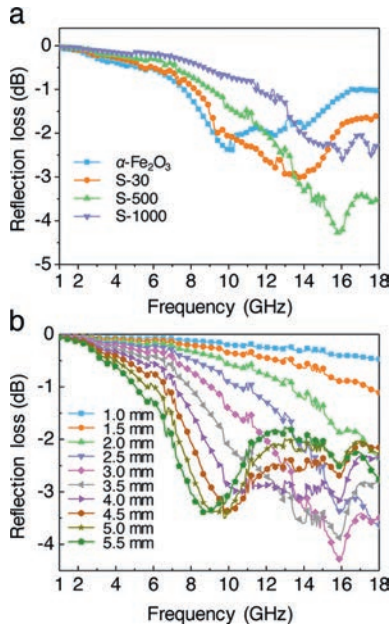

Fig. 4. Microwave absorption performances. (a) R_L curves of α-Fe_2O_3, S-30, S-500, and S-1000 under d of 3.0 mm. (b) R_L curves of S-500 with different d in the range of 1.0~5.5 mm.

shell structure [43-46]. However, the "structure-performance" relationship between shell thickness and microwave absorption performance is rarely reported.

Herein, we have synthesized the core-shell structural α-Fe_2O_3@SiO_2 nanoparticles with a constant core size and changeable shell thickness to explore the "structure-performance" relationship between shell thickness and microwave absorption performance. The dependence of shell thickness on microwave absorption performance and the corresponding mechanisms were revealed and explained, respectively. The results indicated that α-Fe_2O_3@SiO_2 of 35 nm shell-thickness presented a significant enhancement of absorption performance compared with that of pure α-Fe_2O_3. Although the absolute value of the reflection loss was relatively low (–4.3 dB), this study has shed an important reference on the design of next-generation advanced iron oxide-based materials for excellent microwave absorption by tuning the shell-thickness. Meanwhile, based on the "structure-performance" relationship between shell-thickness and microwave absorption performance, the Fe@SiO_2, γ-Fe_2O_3@SiO_2, Fe_3O_4@SiO_2, and FeNx@SiO_2 with excellent absorption performance will also be fabricated/developed from the core-shell structural α-Fe_2O_3@SiO_2 nanoparticles by phase conversion of α-Fe_2O_3 through heat treatment.

The core-shell structural α-Fe_2O_3@SiO_2 nanoparticles were synthesized through the Stöber method (Fig. S1 in Supporting information) [47,48]. By controlling the mass of tetraethyl orthosilicate (TEOS) during this reaction, the shell-thickness of SiO_2 was finely regulated in the range of 0-190 nm (Fig. 1). Pure α-Fe_2O_3 cores present a uniformly dispersed size with 50 ± 10 nm (Figs. 1a and b, Fig. S2 in Supporting information). The lattice space of 0.27 nm corresponds to the (104) lattice plane of α-Fe_2O_3 (Fig. 1b). With increasing the mass of TEOS from 30 to 2000 mg, the shell-thickness of SiO_2 increases from 6 ± 2 nm to more than 190 nm (Figs. 1a-t). Specifically, when the TEOS mass is less than 200 mg, the α-Fe_2O_3@SiO_2 nanoparticles are granular (Figs. 1c-j). Then with increasing TEOS from 200 to 500 mg, the morphology of α-Fe_2O_3@SiO_2 tends to be a sphere with a single core (Figs. 1k-n). And further increasing TEOS mass to 2000 mg, the agglomeration of α-Fe_2O_3 cores would be induced in α-Fe_2O_3@SiO_2 particles (Figs. 1o-t, Fig. S3 in Supporting information). Based on the relationship between shell-thickness and TEOS mass, we can infer the shell growth rate is 0.091 nm/$mg_{(TEOS)}$, *i.e.*, each 1 mg TEOS can increase the shell-thickness by 0.091 nm (Fig. S4 in Supporting information). This SiO_2 shell growth rate maybe provides an important data reference for the fine synthesis of other core-shell structural M@SiO_2 (M = metal oxides, metal particles, carbon materials, *etc.*) nanomaterials.

Typically, the structure and components of α-Fe_2O_3, S-30, S-500, and S-1000 were characterized in detail (Fig. 2). Pristine α-Fe_2O_3 nanoparticle presents a series of X-ray diffraction (XRD) peaks at 24.1°, 33.1°, 35.6°, 40.9°, 49.5°, 54.09°, 57.59°, 62.45°, 63.99°, 71.94°, and 75.43°, corresponding to the (012), (104), (110),

(113), (024), (116), (018), (214), (300), and (1010) lattice planes (JCPDS No. 33-0664) (Fig. 2a). These sharp and strong diffraction peaks indicate that the pristine α-Fe_2O_3 nanoparticles have high crystallinity and purity. When the added mass of TEOS was less than 500 mg, the as-prepared samples, *i.e.*, S-30 and S-500, exhibit similar diffraction peaks with pristine α-Fe_2O_3, and no obvious SiO_2 characteristic peak appeared due to the amorphous form of SiO_2 shell. When the TEOS mass was 1000 mg, the amorphous SiO_2 characteristic peak around 20°~30° began to appear in the corresponding sample, *i.e.*, S-1000. The existence of SiO_2 in S-500 and S-30 samples could be confirmed by Fourier transform infrared spectroscopy (FT-IR), X-ray photoelectron spectroscopy (XPS), and elemental mappings (Figs. 2b-j, Fig. S5 in Supporting information). For the S-500 sample, FT-IR absorption peaks at 1097, 949, and 789 cm^{-1} were caused by Si-O-Si, Si-OH, and Si-O vibrations from the SiO_2 shell (Fig. S5 in Supporting information). After coating of the SiO_2 shell, Fe 2p and Fe 3p peaks in XPS full spectra almost disappeared, but Si 2p and Si 2s appeared (Figs. 2b and c). Compared with pristine α-Fe_2O_3, the Fe $2p_{3/2}$, and Fe $2p_{1/3}$ peaks of S-500 all shifted to higher binding energy by *ca.* 0.4 eV in XPS fine spectra, confirming the interaction between α-Fe_2O_3 core and SiO_2 shell (Fig. 2d). These results indicate the presence of SiO_2-shell layers in S-500 [49,50]. In order to further visually observe the core-shell structure, the S-30 sample with thin SiO_2 layers was selected for elemental mapping characterization (Figs. 2e-j). Element mappings demonstrated that the outer shell layers were dominated by Si and O, and the inter cores by Fe and O (Figs. 2f-j).

The static magnetic properties of as-prepared α-Fe_2O_3@SiO_2 nanoparticles were measured using a vibrating sample magnetometer (VSM). For pure α-Fe_2O_3, it does not reach saturation magnetization even under a very high applied magnetic field of –80~80 kOe, suggesting its weak ferromagnetic behavior [35,37,51] (Fig. S6 in Supporting information). Therefore, the α-Fe_2O_3@SiO_2 samples also do not reach saturation magnetization, and only possess narrow hysteresis features (Fig. S7 in Supporting information). Among them, the S-500 sample has a maximum area indicating higher hysteresis loss of energy. The detailed remanent magnetization (M_r) and coercivity (H_c) values of these samples were summarized in Table S1 (Supporting information). With increasing SiO_2-shell thickness, M_r and H_c first increase and then decrease. The M_r value increases from 0.030 emu/g (for pure α-Fe_2O_3) to 0.045 emu/g (for S-500), then decreases to 0.022 emu/g (for S-1000). Similarly, the H_c value increases from 71 Oe to 1100 Oe, then decreases to 458 Oe (Table S1). The first increment resulted from the internal stress on the core generated by the shell, which hindered the rotation of the magnetic domain during the magnetization process [7,52]. The subsequent decline was attributed to the fact that quite large amount of non-magnetic SiO_2 shell layer reduced the content of α-Fe_2O_3 core. Besides, whether the agglomeration of α-Fe_2O_3 cores in single particles leads to the deterioration of H_c still needs further study (Fig. S7 in Supporting information).

For microwave absorbing materials, the electromagnetic parameters, *i.e.*, relative complex permittivity ($\varepsilon_r = \varepsilon_r' + \varepsilon_r''$) and relative complex permeability ($\mu_r = \mu_r' + \mu_r''$), directly influence their microwave absorbing performances. The real parts (ε_r' and μ_r') represent the storage capability of electric and magnetic energy, and the imaginary parts (ε_r'' and μ_r'') represent the loss ability of electric and magnetic energy [21,53]. Specifically, with increasing thickness of the SiO_2 shell, the ε_r' values of these four samples gradually decreased from *ca.* 5.7 to *ca.* 3.5, in the order of α-Fe_2O_3 > S-30 > S-500 > S-1000 (Fig. 3a). Finally, the ε_r' value of S-1000 was close to that of bulk SiO_2 (*ca.* 4.0), due to the ~90 nm thick insulating layer of SiO_2 [54]. However, with the increase of SiO_2-shell thickness, the ε_r'' values first increased and then decreased (Fig. 3b). The corresponding dielectric loss tangent ($\tan\delta_\varepsilon = \varepsilon_r''/\varepsilon_r'$) values also presented a similar evolution, from 0.02 (α-Fe_2O_3) to 0.08 (S-500), then to 0.06 (S-1000) (Fig. 3c). The evolutions of ε_r' and $\tan\delta_\varepsilon$ may be due to the influence of SiO_2-shell thicknesses, which was explained in the section for relationships of "structure-performance". For relative complex permeability, with increasing the SiO_2-shell thickness, the μ_r' values in these four samples ranged from 0.99 to 1.13 (Fig. 3d), and the μ_r'' values presented a gradually decreasing trend from 0.08 to 0.02 (Fig. 3e). The corresponding magnetic loss tangent ($\tan\delta_\mu = \mu_r''/\mu_r'$) values gradually decreased from 0.08 (α-Fe_2O_3) to 0.02 (S-1000), indicating the decrease of magnetic loss capability (Fig. 3f). Compared with the electromagnetic parameters, *i.e.*, relative complex permittivity and relative complex permeability, the values of ε_r', ε_r'' and $\tan\delta_\varepsilon$ were all higher than those of μ_r', μ_r'' and $\tan\delta_\mu$. This result indicated that the contributions of dielectric loss were more than that of magnetic loss in the microwave absorption process.

In general, the dielectric loss of material stems from conduction loss and polarization loss (*e.g.* ionic polarization, electric polarization, dipolar polarization, and interfacial polarization) [55,56]. In our case, the ionic polarization and electron polarization would be excluded, because they generally exist in a much higher frequency region (103~106 GHz) [54]. Wave-like shapes of the curves were a typical behavior of dielectric relaxation (Figs. 3a-c), which was responsible for intrinsic dipolar polarization of the core structure [55,57]. Generally, the insulator SiO_2 possesses lower conductivity than that of the semiconductor α-Fe_2O_3. With the increase of SiO_2 content, the reduced conductivity of α-Fe_2O_3@SiO_2 led to the degradation of ε_r' (Fig. 3a). According to the equation ($\varepsilon_r'' \approx \sigma/(2\pi\varepsilon_0 f)$, where σ is the conductivity, ε_0 is the permittivity in the free space, and f is the frequency), the ε_r'' theoretically should also decrease with the reduced conductivity [3,34]. However, the ε_r'' of core-shell structural α-Fe_2O_3@SiO_2 nanoparticles (S-30 and S-500) was higher than that of pure α-Fe_2O_3 (Fig. 3b). The phenomena may be possibly attributed to the compensation effect from the interfacial polarization, which originates from the charge buildup around the core-shell interface [7,53,55]. Therefore, the variations feature of dielectric loss of α-Fe_2O_3@SiO_2 samples came from the dipolar polarization of the core structure, decrease of overall conductivity, and introduction of interfacial polarization.

Microwave absorption performances of α-Fe_2O_3@SiO_2 nanoparticles can be evaluated by the reflection loss (R_L), which is derived from the following formulas [58,59].

$$Z_{in} = Z_0\sqrt{\frac{\mu_r}{\varepsilon_r}}\tanh\left[j\left(\frac{2\pi fd}{c}\right)\sqrt{\varepsilon_r\mu_r}\right] \quad (1)$$

$$R_L(\mathrm{dB}) = 20\log\left|\frac{Z_{in}-Z_0}{Z_{in}+Z_0}\right| \quad (2)$$

where Z_0 is the characteristic impedance of free space, Z_{in} is the input impedance of the microwave absorber, d is the thickness of the absorber, c is the speed of light, and f is the frequency of the microwave. Using the measured electromagnetic parameters in Fig. 3, the R_L of core-shell structural α-Fe_2O_3@SiO_2 nanoparticles with different shell thicknesses can be calculated from formulas 1and 2.

To more clearly reflect the influence of SiO_2-shell thickness, the R_L of α-Fe_2O_3@SiO_2 nanoparticles with fixed d (sample thickness) of 3.0 mm were evaluated in Fig. 4a. With increasing the SiO_2-shell thickness, the minimum value of R_L first decreased and then increased (Fig. 4a). S-500 sample possessed the strongest microwave absorption with the lowest R_L value of –4.3 dB. Thus, the microwave absorption performance of α-Fe_2O_3@SiO_2 would be enhanced under proper SiO_2-shell thickness. Fig. 4b shows the performances of S-500 under different d of 1.0~5.5 mm. As d was in the range of 1.0~2.0 mm, the R_L decreased monotonously with the increase of frequency from 1~18 GHz. In the range of 2.5~5.5 mm, each curve presented a sharp or broad peak. As d was 3.0 mm, the

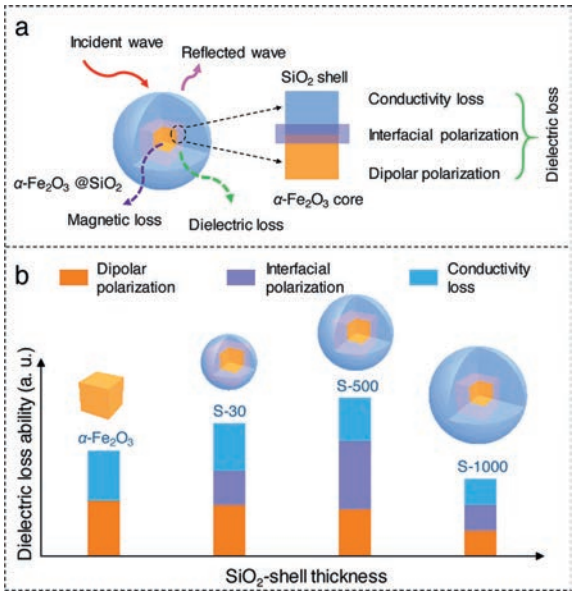

Fig. 5. The "structure-performance" relationships. (a) Schematic of the possible microwave absorbing mechanism. (b) The evolution of the dielectric loss ability with the increase of SiO_2-shell thickness.

R_L achieved the minimum value of –4.3 dB at 16 GHz, which was superior to that of pure α-Fe_2O_3 (Fig. 4b and Fig. S8 in Supporting information). Additionally, it is interesting to note that most of the strong peaks were constrained in 6~11 and 13~17 GHz. This phenomenon may be generated from the wave character of dielectric loss (Figs. 3b, c and 4b).

Fig. 5 illustrates the analysis of "structure-performance" relationships in the core-shell structural α-Fe_2O_3@SiO_2 nanoparticles. Based above results, the microwave absorption performances for the α-Fe_2O_3@SiO_2 nanoparticles mainly come from the dielectric loss rather than the magnetic loss. The evolution of dielectric loss is mainly influenced by three factors: dipolar polarization of the α-Fe_2O_3 core, interfacial polarization between α-Fe_2O_3 core and SiO_2 shell, and conductivity loss from the α-Fe_2O_3 core (Fig. 5a). The former factor may lead to the wave-like shapes of curves ε', ε_r'' and tan δ_ε, and the others will be conducive for the microwave absorption enhancement. Therefore, the microwave absorption performance of α-Fe_2O_3@SiO_2 can be adjusted by tuning the SiO_2-shell thickness, and achieve the best under a proper SiO_2-shell thickness (Fig. 5b).

Specifically, for the pure α-Fe_2O_3 nanoparticle, there are dipolar polarization and conductivity loss contributing to the dielectric loss. Although the dipolar polarization interaction and conductivity loss slightly decrease with the slight increase of the SiO_2-shell thickness, the appearances of interfacial polarization lead to an enhancement of the overall dielectric loss ability, *e.g.*, the case of S-30 (Fig. 5b). With the continuous increase of the SiO_2-shell thickness, *e.g.*, the case from S-30 to S-500, the contributions of both dipolar polarization and conductivity loss all gradually decrease. But the interfacial polarization continuously increases so that the dielectric loss ability reaches the optimum level at a proper SiO_2-shell thickness, *i.e.*, in the case of S-500 (Fig. 5b). Further increasing the thickness of SiO_2 shells, *e.g.*, the case from S-500 to S-1000, the dipolar polarization, interfacial polarization, and conductivity loss all gradually decrease to the minimum, *e.g.*, the case of S-1000. It is due to the mismatched thickness of SiO_2 insulation layers resulting in that the overall dielectric loss ability presents a decreased trend and unlimitedly approaches to that of pure SiO_2 nanoparticles (Fig. 5b) [54]. Therefore, at the proper SiO_2-shell thickness of 35 nm, the S-500 sample achieved the strongest microwave absorbing ability.

In summary, we have synthesized the core-shell structural α-Fe_2O_3@SiO_2 nanoparticles with a constant α-Fe_2O_3-core size and changeable SiO_2-shell thickness to explore the "structure-performance" relationship between shell thickness and microwave absorption performance. The shell thickness increases nearly linearly as the TEOS addition increases, with a slope of about 0.091 $nm/mg_{(TEOS)}$. There is a strong "structure-performance" dependence between microwave absorption performance and SiO_2-shell thickness. With increasing the SiO_2-shell thickness, the microwave absorption ability first increase and then decrease. This indicates that the microwave absorption performance of α-Fe_2O_3@SiO_2 can be enhanced under proper SiO_2-shell thickness. With a proper SiO_2-shell thickness of 35 nm, the S-500 sample achieved the strongest microwave absorbing ability with a minimum R_L value of –4.3 dB under a sample thickness of 3 mm, higher than that of pure α-Fe_2O_3 (–3.8 dB with 2.5 mm). This enhanced microwave absorption performance is mainly derived from dielectric loss including conductivity loss, interfacial polarization, and dipolar polarization. Although the absolute value of the reflection loss was relatively low (–4.3 dB), this study shed an important reference on designing next-generation advanced iron oxide-based materials for microwave absorption by tuning the shell thickness. Meanwhile, based on the "structure-performance" relationship between SiO_2-shell thickness and microwave absorption performance, the M@SiO_2 (M = Fe, γ-Fe_2O_3, Fe_3O_4 and FeN_x) with excellent absorption performance will also be fabricated/developed from the core-shell structural α-Fe_2O_3@SiO_2 nanoparticles by phase conversion of α-Fe_2O_3 through heat treatment.

Declaration of competing interest

The authors declare no conflict of interest.

Acknowledgments

This work was financially supported by the National Natural Science Foundation of China (Nos. 21667019, 22066017, 52001156, and 52000163), the Key Project of the Natural Science Foundation of Jiangxi Province (No. 20171ACB20016), the Jiangxi Province Major Academic and Technical Leaders Cultivating Object Program (No. 20172BCB22014), the Science and Technology Department of Jiangxi Province (Nos. 20181BCB18003, 20181BAB216012, 20181ACG70025, CK202002473, and 20192BAB216003), the Key Laboratory of Photochemical Conversion and Optoelectronic Materials, TIPC, CSA (No. PCOM201906), and the Key Project of Science and Technology Research of the Jiangxi Provincial Department of Education (Nos. DA201602063, GJJ191044), the Aviation Science Foundation of China (No. 2017ZF56020) and the Program B for Outstanding Ph.D. Candidate of Nanjing University (No. 202002B076), and the Natural Science Foundation of Henan Province (No. 202300410423).

Supplementary materials

Supplementary material associated with this article can be found, in the online version, at doi:10.1016/j.cclet.2021.07.027.

References

[1] S. Li, Q. Li, J. Xu, et al., Adv. Funct. Mater. 26 (2016) 3738–3744.
[2] M. Javid, Y. Zhou, D. Wang, et al., ACS Appl. Nano Mater. 1 (2018) 1309–1320.
[3] J. Luo, K. Zhang, M. Cheng, M. Gu, X. Sun, Chem. Eng. J. 380 (2020) 122625.
[4] R. Peymanfar, A. Ahmadi, E. Selseleh-Zakerin, J. Alloys Compd. 848 (2020) 156453.
[5] Z. Jia, D. Lan, K. Lin, et al., J. Mater. Sci.: Mater. Electron. 29 (2018) 17122–17136.
[6] B. Qu, C. Zhu, C. Li, X. Zhang, Y. Chen, ACS Appl. Mater. Interfaces 8 (2016) 3730–3735.

[7] G. Liu, L. Wang, Z. Yang, R. Wu, J. Alloys Compd. 718 (2017) 46–52.
[8] J. Zhao, Y. Xie, D. Guan, et al., Sci. Rep. 5 (2015) 12544.
[9] L. Sha, P. Gao, T. Wu, Y. Chen, ACS Appl. Mater. Interfaces 9 (2017) 40412–40419.
[10] T. Liu, Y. Pang, M. Zhu, S. Kobayashi, Nanoscale 6 (2014) 2447–2454.
[11] Q. Liu, Z. Zi, D. Wu, Y. Sun, J. Dai, J. Mater. Sci. 47 (2011) 1033–1037.
[12] V.D. Phadtare, V.G. Parale, T. Kim, et al., J. Alloys Compd. 823 (2020) 153847.
[13] P. Liu, V.M.H. Ng, Z. Yao, et al., ACS Appl. Mater. Interfaces 9 (2017) 16404–16416.
[14] V.D. Phadtare, V.G. Parale, G.K. Kulkarni, H.H. Park, V.R. Puri, Ceram. Int. 44 (2018) 7515–7523.
[15] Y. Song, F. Yin, C. Zhang, et al., Nano-Micro Lett. 13 (2021) 76.
[16] X. Lin, J. Wang, Z. Chu, et al., Chin. Chem. Lett. 31 (2020) 1124–1128.
[17] Y. Zhang, Y. Huang, T. Zhang, et al., Adv. Mater. 27 (2015) 2049–2053.
[18] J. Zhao, Y. Xie, Z. Le, et al., Synthetic Met 181 (2013) 110–116.
[19] R. Yang, X. Gui, L. Yao, et al., Nano-Micro Lett. 13 (2021) 66.
[20] Y. Jiang, X. Fu, Z. Zhang, et al., J Mater. Sci.: Mater. Electron. 30 (2019) 19173–19181.
[21] C. Tian, Y. Du, P. Xu, et al., ACS Appl. Mater. Interfaces 7 (2015) 20090–20099.
[22] N. Mokhtar, P.Y. Wong, G.B. Teh, S.W. Phang , Polym. Bull. 78 (2021) 6351–6365.
[23] J. Zhao, Y. Xie, Z. Le, et al., Polym. Compos. 34 (2013) 1801–1808.
[24] J. Luo, L. Yue, H. Ji, K. Zhang, N. Yu, J. Mater. Sci. 54 (2019) 6332–6346.
[25] Y. Wang, X. Di, Z. Lu, X. Wu, J. Colloid Interface Sci. 589 (2021) 462–471.
[26] J. Sun, Y. Shen, X.S. Hu, Polym. Bull. 75 (2018) 653–667.
[27] J.M.A. Sulaiman, M.M. Ismail, S.N. Rafeeq, Appl. Phys. A 126 (2020) 236.
[28] X. Zhao, Y. Huang, J. Yan, et al., J. Colloid Interface Sci. 595 (2021) 78–87.
[29] J. Zhao, Y. Xie, C. Yu, et al., Mater. Chem. Phys. 142 (2013) 395–402.
[30] X. Di, Y. Wang, Y. Fu, X. Wu, P. Wang, Carbon 173 (2021) 174–184.
[31] X. Zhao, Y. Huang, J. Yan, et al., Compos. Sci. Technol. 210 (2021) 108801.
[32] K. Jia, R. Zhao, J. Zhong, X. Liu, J. Magn. Magn. Mater. 322 (2010) 2167–2171.
[33] B. Lu, X.L. Dong, H. Huang, et al., J. Magn. Magn. Mater. 320 (2008) 1106–1111.
[34] P. Liu, S. Gao, Y. Wang, et al., ACS Appl. Mater. Interfaces 11 (2019) 25624–25635.
[35] J. Lian, X. Duan, J. Ma, et al., ACS Nano 3 (2009) 3749–3761.
[36] S. Cao, Y. Zhu, G. Cheng, Y. Huang, J. Phys. Chem. Solids 71 (2010) 1680–1683.
[37] H. Jiao, G. Jiao, Mater. Lett. 63 (2009) 2725–2727.
[38] X. Zheng, J. Cai, W. Zhao, et al., Chin. Chem. Lett. 32 (2021) 2143–2150.
[39] B. Paul, S. Vadivel, S.S. Dhar, Chin. Chem. Lett. 27 (2016) 1725–1730.
[40] H. Nagabhushana, S.S. Saundalkar, L. Muralidhar, et al., Chin. Chem. Lett. 22 (2011) 143–146.
[41] M. Wang, M. Wang, Y. Fu, S. Shen, Chin. Chem. Lett. 28 (2017) 2207–2211.
[42] Z. Zhu, L. Zhong, Y. Wang, G. Zeng, W. Wang, Chin. Chem. Lett. 31 (2020) 2619–2622.
[43] M. Feyen, C. Weidenthaler, R. Guttel, et al., Chem. Eur. J. 17 (2011) 598–605.
[44] Z.M. Cui, Z. Chen, C.Y. Cao, L. Jiang, W.G. Song, Chem. Commun. 49 (2013) 2332–2334.
[45] X. Guo, Y. Deng, D. Gu, R. Che, D. Zhao, J. Mater. Chem. 19 (2009) 6706–6712.
[46] J. Xu, J. Liu, R. Che, et al., Nanoscale 6 (2014) 5782–5790.
[47] W. Stober, A. Fink, E. Bohn, J. Colloid Interface Sci. 26 (1968) 62–69.
[48] J. Ge, L. Liu, Y. Cui, et al., Ceram. Int. 46 (2020) 15325–15332.
[49] H. Lv, X. Liang, Y. Cheng, et al., ACS Appl. Mater. Interfaces 7 (2015) 4744–4750.
[50] A.L. Morel, S.I. Nikitenko, K. Gionnet, et al., ACS Nano 2 (2008) 847–856.
[51] M. Tadic, N. Citakovic, M. Panjan, et al., J. Alloys Compd. 543 (2012) 118–124.
[52] L. Yan, J. Wang, X. Han, et al., Nanotechnology 21 (2010) 095708.
[53] Y. Du, W. Liu, R. Qiang, et al., ACS Appl. Mater. Interfaces 6 (2014) 12997–13006.
[54] R.R. Mishra, A.K. Sharma, Compos. Part A 81 (2016) 78–97.
[55] B. Quan, X. Liang, G. Ji, et al., J. Alloys Compd. 728 (2017) 1065–1075.
[56] N. Wu, C. Liu, D. Xu, et al., ACS Sustainable Chem. Eng. 6 (2018) 12471–12480.
[57] H.J. Yang, W.Q. Cao, D.Q. Zhang, et al., ACS Appl. Mater. Interfaces 7 (2015) 7073–7077.
[58] H. Sun, R. Che, X. You, et al., Adv. Mater. 26 (2014) 8120–8125.
[59] B. Zhang, Y. Feng, J. Xiong, Y. Yang, H. Lu, IEEE Trans. Magn. 42 (2006) 1778–1781.